






## Holistic yield modeling, top-down loss analysis, and efficiency potential study of thin-film solar modules

Mario Zinßer <sup>1,2</sup>✉, Tim Helder <sup>1,2</sup>, Theresa Magorian Friedlmeier <sup>1</sup>, Andreas Bauer<sup>1</sup>, Thomas Kirchartz <sup>3,4</sup>, Uwe Rau <sup>3</sup>, Rolf Wächter<sup>5</sup> & Michael Powalla<sup>1,2</sup>

A holistic simulation of a photovoltaic system requires multiple physical levels - the optoelectronic behavior of the semiconductor devices, the conduction of the generated current, and the actual operating conditions, which rarely correspond to the standard testing conditions (STC) employed in product qualification. We present a holistic simulation approach for all thin-film photovoltaic module technologies that includes a transfer-matrix method, a drift-diffusion model to account for the p-n junction, and a quasi-three-dimensional finite-element Poisson solver to consider electrical transport. The evolved digital model enables bidirectional calculation from material parameters to non-STC energy yield and vice versa, as well as accurate predictions of module behavior, time-dependent top-down loss analyses and bottom-up sensitivity analyses. Simple input data like current-voltage curves and material parameters of semiconducting and transport layers enables fitting of otherwise less-defined values. The simulation is valuable for effective optimizations, but also for revealing values for difficult-to-measure parameters.

<sup>1</sup>Zentrum für Sonnenenergie- und Wasserstoff-Forschung Baden-Württemberg (ZSW), Meitnerstraße 1, 70563 Stuttgart, Germany. <sup>2</sup>Light Technology Institute (LTI), Karlsruhe Institute of Technology (KIT), Engesserstraße 13, 76131 Karlsruhe, Germany. <sup>3</sup>IEK5-Photovoltaik, Forschungszentrum Jülich, 52425 Jülich, Germany. <sup>4</sup>Faculty of Engineering and CENIDE, University of Duisburg-Essen, Carl-Benz-Str. 199, 47057 Duisburg, Germany. <sup>5</sup>NICE Solar Energy GmbH, Alfred-Leikam-Str. 25, 74523 Schwäbisch Hall, Germany. ✉email: [mario.zinsser@zsw-bw.de](mailto:mario.zinsser@zsw-bw.de)

The world's annually rising primary energy consumption<sup>1,2</sup> correlates with increasing CO<sub>2</sub> emissions and climate change<sup>3</sup>. Meeting the demand while reducing emissions requires scientific research, industrial production, and finally, a very large installation volume of environmentally friendly electricity generation technologies<sup>4</sup>. Thin-film solar modules for photovoltaic energy generation combine high cell efficiencies<sup>5–7</sup>, short energy payback times due to low consumption of energy and active material<sup>8,9</sup>, and potential for cheap monolithic and large-scale manufacturing at moderate temperatures<sup>10–12</sup>. Further advantages like integration into efficient tandem applications<sup>13–16</sup>, their possibility for ink-based fabrication techniques<sup>17</sup>, their application in photoelectrochemical (PEC) hydrogen production<sup>14,18,19</sup>, and the feasibility for flexible substrates<sup>13,20–22</sup> make thin-film technology a promising candidate for many different applications.

In order to keep pace with the current market-dominating c-Si technology<sup>23,24</sup>, thin-film technologies need to have comparably high efficiencies. The best way to systematically analyze the internal physical processes is automated computer-aided modeling approaches<sup>25</sup>. Therefore, thin-film solar devices are under frequent investigation by computer simulation, both by electrical simulations<sup>26–28</sup> as well as by drift-diffusion models<sup>29,30</sup>. To not only guide development efforts towards increased efficiencies but also to higher net energy yields, entire modules in the field need to be investigated instead of single cells in the laboratory<sup>31,32</sup>. Real-world simulations identify, allocate, quantify, and rate all loss mechanisms within thin-film solar modules. It is important to put in proportion all identified losses<sup>33</sup>. Hence, a holistic simulation method including all loss mechanisms from the Shockley–Queisser model<sup>34,35</sup> down to the actual produced module power is necessary. This requires a linkage of at least three simulation levels, as realized in this unique simulation platform. Therefore, we connected an electronic drift–diffusion model<sup>29</sup> within a one-dimensional finite element method for the semiconductor material simulation, a modified transfer-matrix approach<sup>36,37</sup> to consider the optics with partially incoherent interference due to rough interfaces<sup>38</sup>, and an electrical Poisson's equation<sup>39</sup> solver embedded into a quasi-three-dimensional finite element method using a Delaunay-triangulated mesh<sup>40,41</sup> to account for the electrical module behavior. Therefore, our methodology includes the entire chain of physical processes within the simulation of solar modules and bridges the gap between cell simulation and system design software. All simulations are programmed by the authors without using any external software. This holistic approach also allows a calculation in the backward direction and therefore allows the inference of material parameters from characteristic curves on the module level, which we will call Reverse Engineering Fitting (REF)<sup>40</sup>. Moreover, our methodology comes with the additional benefit that possible research improvements can be checked for their contribution to the overall module performance, revealing insightful sensitivity analyses. Furthermore, solar power plant operators often face the question of financial return. While the investment costs in €/kW<sub>p</sub> can be calculated easily, the yield per time in kWh per a depends e.g., on the climate conditions of the specific system location. Advanced simulation techniques like this work offer the possibility to calculate such quantities. Furthermore, the effect of technological improvements can be evaluated much better, and therefore, priorities can be set in the research and development process.

In the photovoltaic market, there is a wide variety of different technologies. While silicon wafer-based photovoltaic is widespread, thin-film systems have great potential for cost-effective energy generation. Thin-film modules with the monolithic interconnection technique are more difficult to simulate than

wafer-based modules. Our simulation methodology works for all thin-film technologies and, in principle, could be modified for wafer-based technologies. We demonstrate our universal approach on the 1.2 × 0.6 m<sup>2</sup> large copper indium gallium selenide CuIn<sub>1–x</sub>Ga<sub>x</sub>Se<sub>2</sub> (CIGS) module N-G1000E105 from NICE Solar Energy GmbH. It consists of 144 monolithically integrated cells and the following layer stack: 400 nm molybdenum (Mo)/2100 nm CIGS/50 nm cadmium sulfide (CdS)/50 nm intrinsic zinc oxide (i-ZnO)/800 nm aluminum-doped zinc oxide (AZO)/750 μm encapsulant film/3.2 mm top side ARC-coated low-iron solar float glass.

In this paper, we demonstrate a holistic approach to simulate solar modules under real conditions. We use a combination of an optical transfer matrix method, an electrical transport simulation, and a drift–diffusion calculation. This allows top-down loss analyses, determining the influence of possible future technology improvements on the yield, and backward calculations from measured data to difficult-to-measure parameters.

## Results

**Evolving the digital model and its parameters under standard testing conditions (STC).** As a first step, all measurable quantities are implemented into the model. This mainly includes geometrical data (layer thicknesses and lateral dimensions), complex refractive indices of all thin-film layers and from the encapsulant layer (for CIGS from literature, for all remaining materials fitted ellipsometry and transmittance measurements), as well as specific resistivities of all contact layers (here AZO and Mo). While there are also other optical data for CIGS in literature<sup>42</sup>, we used the data from<sup>43</sup>, since we found a very good agreement of simulated and measured external quantum efficiencies. Moreover, a sensitivity analysis reveals that the exact absorption coefficient of the CIGS layer is not very sensitive for a sufficiently large layer thickness if the band gap matches the experimental value. To properly execute drift-diffusion simulations, several semiconductor parameters of the photo-active layers from the literature are implemented as well. They are listed in Table 1.

In Fig. 1, the black points represent the measured current–voltage (*I*–*V*) characteristic of the module, broken down into a single monolithically integrated cell. The consistently equal shunting effect up to the 0.5 V range without having a larger slope at higher voltages reveals the homogeneity of all cells within the module<sup>44</sup>. Otherwise, a dip in the current could be seen at higher voltages<sup>45</sup>. It justifies the approach of a sufficiently homogeneous p–n junction without pronounced hot-spot shunt regions in individual cells.

After we accounted for the electrical, geometrical, and optical losses (orange, green, and blue curves), we performed a Reverse Engineering Fitting (REF) procedure<sup>40</sup> for all difficult-to-measure parameters at standard testing conditions (STC) (meaning 1000 W m<sup>–2</sup> irradiance, 25 °C module temperature, and AM1.5G spectral distribution) throughout all simulation levels down to the drift-diffusion model. These parameters are the donor and acceptor densities and electron and hole mobilities. More information about the REF procedure can be found in the methods section. Using this multi-level REF method, we are able to determine the quantities of donor and acceptor densities and the charge carrier mobilities within the CIGS and CdS layers, which are experimentally difficult to access. These results can be seen as bold numbers in Table 1. The fitted donor density within the CdS and the acceptor density within the CIGS turn out to be on a comparable level with values found in literature<sup>46–50</sup> within the 10<sup>17</sup>  $\frac{1}{\text{cm}^3}$  and 10<sup>15</sup>  $\frac{1}{\text{cm}^3}$  range, respectively. However, we found evidence for a noticeably higher electron mobility within the CIGS layer of  $\mu_e = 200 \frac{\text{cm}^2}{\text{Vs}}$  instead of the commonly used value of 100  $\frac{\text{cm}^2}{\text{Vs}}$ <sup>47–51</sup>, which is often just a estimation in a plausible order

**Table 1 Semiconductor parameters for drift-diffusion modeling. The material abbreviations CIGS, CdS, i:ZnO, and AZO stand for copper indium gallium diselenide, cadmium sulfide, intrinsic zinc oxide, and aluminum-doped zinc oxide, respectively. All bold numbers are fitted via reverse engineering fitting procedure from the measured module I-V characteristic, all others are adapted from literature. The CIGS absorber material has a linear grading within the ratio of gallium to gallium and indium concentrations  $[Ga]/([Ga]+[In])$  (GGI) of 0.2 to 0.4. Detailed conversions into an absorber band gap can be found in Supplementary Note 1 and band gap or in literature<sup>69,70</sup>.**

		CIGS	CdS	i:ZnO	AZO
Thickness	$d/\text{nm}$	2100	50	50	800
Band gap	$E_{\text{gap}}/\text{eV}$	1.13-1.25	2.4	3.3	3.3
Chemical potential	$\chi/\text{eV}$	4.5	4.2	4.45	4.45
Relative permittivity	$\epsilon_r$	12.9	10	9	9
Effective conduction band density of states at 300 K	$N_c/\frac{1}{\text{cm}^3}$	$2.2 \times 10^{18}$	$2.2 \times 10^{18}$	$2.2 \times 10^{18}$	$2.2 \times 10^{18}$
Effective valence band density of states at 300 K	$N_v/\frac{1}{\text{cm}^3}$	$1.8 \times 10^{19}$	$1.8 \times 10^{19}$	$1.8 \times 10^{19}$	$1.8 \times 10^{19}$
Donor density	$N_D/\frac{1}{\text{cm}^3}$	-	$1 \times 10^{17}$	-	$1 \times 10^{19}$
Acceptor density	$N_A/\frac{1}{\text{cm}^3}$	$3 \times 10^{15}$	-	-	-
Electron mobility	$\mu_e/\frac{\text{cm}}{\text{Vs}}$	<b>200</b>	<b>100</b>	100	100
Hole mobility	$\mu_h/\frac{\text{cm}}{\text{Vs}}$	<b>25</b>	<b>25</b>	25	25

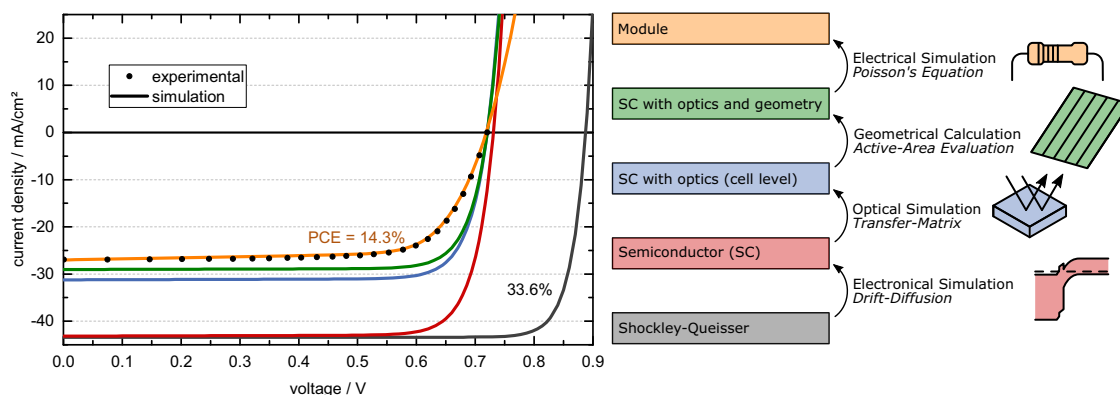


**Fig. 1 All relevant I-V characteristics from Shockley-Queisser model to the actual module curve.** The gray curve is the I-V characteristic of the Shockley-Queisser model for the band gap of the used module (1.13 eV). After performing a stand-alone drift-diffusion simulation with the parameters from Table 1, we end up at the red curve. The blue curve arises after further subtracting all optical losses and represents the infinitesimal small cell level. For the green curve, we included all geometrical losses of the module, and the orange curve emerges after electrical stimulation and represents the final result for the module I-V characteristic of the stacked simulation. It has a power conversion efficiency (PCE) of 14.3%. The black dotted curve shows actual measurements of the module.

of magnitude since a reasonable measurement is rather difficult to execute. This results in a higher electron diffusion length  $L_e = \sqrt{\mu_e \tau k_B T / q_e}$  at a given temperature  $T$ , a charge carrier lifetime  $\tau$ , the Boltzmann constant  $k_B$ , and the electron charge  $q_e$ .

In summary, we developed a holistic model of a real-world solar module accounting for all dominant loss mechanisms by combining an electronic drift-diffusion model within a one-dimensional finite element method (FEM), an optical transfer-matrix model (TMM), and a quasi-three-dimensional FEM solving the electrical Poisson’s equation. All models are described in more detail in the methods section and in Supplementary Note 2. The models are fed by experimentally measured data, data from the literature, and reverse engineering fitted data. This entirely holistic model enables us to calculate from the Shockley-Queisser limit<sup>34</sup> of the 1.13 eV CIGS absorber down to the module level.

Figure 1 shows the I-V characteristics under STC of all intermediate steps. While the short-circuit current density  $j_{sc}$  remains constant within the drift-diffusion simulation from the Shockley-Queisser model to the semiconductor level, the open-circuit voltage  $V_{oc}$  is drastically decreased due to non-radiative recombination<sup>52</sup>, which is even the case for high-performance

cells<sup>53</sup>. The optical TMM simulation reduces  $j_{sc}$  due to reflection and parasitic and incomplete absorption. Since  $V_{oc}$  logarithmically depends on the photocurrent, it is slightly decreased as well. This blue line is often referred to as the cell level since only vertical optoelectronic effects and no lateral transport effects are considered to this point. To account for the module geometry, edge areas and interconnect areas are introduced, generating the green curve. The new I-V curve is calculated via a comparison of the active and inactive areas. Finally, the current collection and transport are taken into account by the quasi-three-dimensional Poisson’s equation solver. This mainly increases the series resistance and the shunt, yielding a lower fill factor. Moreover, the short-circuit current density is reduced. This is due to the effect of additional shunting resistance and local maximum power point (MPP) mismatches<sup>54</sup>. The latter arises from a non-equal voltage distribution across the cell. This leads to different points of operation within the material’s I-V characteristic for different spatial locations, and only a minority of them are exactly at the cell’s MPP<sup>40</sup>.

The finally predicted I-V characteristic under STC (orange curve in Fig. 1) has a coefficient of determination of 0.997 with respect to the experimentally measured I-V curve (black dots), revealing the high accuracy of our model.

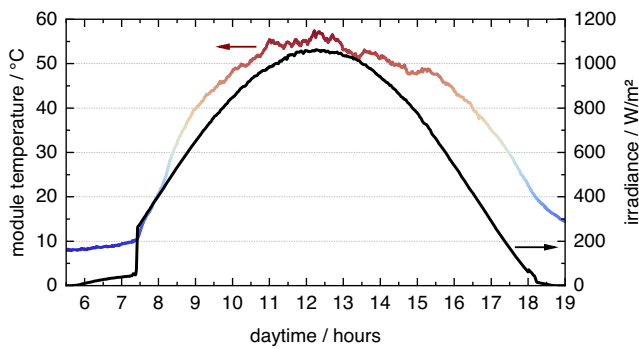


**Fig. 2 External conditions on the solar module during the daytime of September 9, 2020.** The irradiance (black line) on the module plane has basically a trigonometrical dependence on the time of day. The drop from 6 am to 7:30 am is due to trees that block the sunlight. The measured module temperature (blue-red line) has the same behavior as the irradiance but lags behind it.

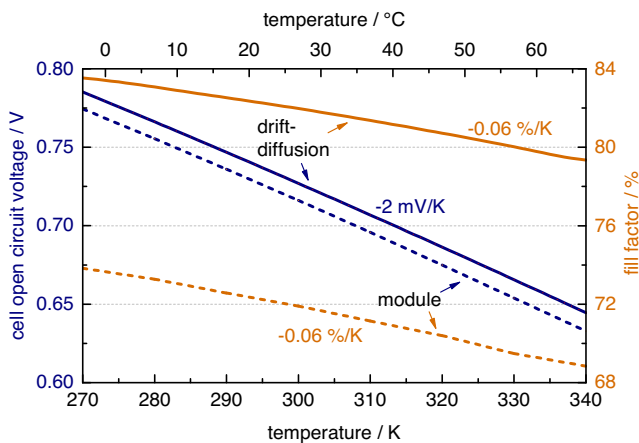


**Fig. 3 Simulated temperature-dependence of the open-circuit voltage and the fill factor.** The solid line represents the results of the drift-diffusion calculation without any optical and electrical losses, while the dashed line shows the overall module behavior. The rising temperature increases the intrinsic carrier concentration and decreases the band gap, which leads to the observed decreasing behavior of the open circuit voltage and the fill factor. The temperature dependence of the short circuit current density and power conversion efficiency can be found in Supplementary Note 3.

**Applying meteorological data to the model.** In order to simulate the daily yield of the module, the incoming irradiance and the module temperature (measured on the rear side of the module) need to be considered. Their course over the day can be seen in Fig. 2. We chose September 9, 2020 as a sample day because it was a clear day with no clouds. The dip at the left of the irradiance graph (black line) at half past 7 arises from locally present trees that cover the low sun at low altitudes in the morning. The module temperature (blue-red line) roughly follows the behavior of the irradiance with a certain delay due to heating.

The effect of the module temperature mainly influences the semiconductor properties within the p–n junction. Therefore, we simulated the p–n junction without lateral electrical effects at different temperatures and the resulting temperature-dependent  $I$ – $V$  characteristic acts as the input for the subsequent Poisson's equation solver. Figure 3 shows the dependence of the open-circuit voltage and the fill factor as a function of the temperature. The solid lines represent the p–n junction simulation results, which are exclusively generated by the drift-diffusion model, whereas the dashed lines represent the overall module behavior, including all

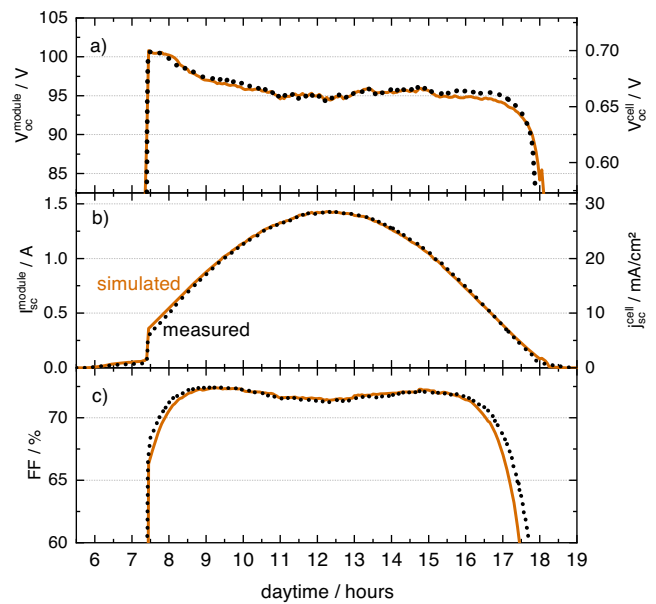


**Fig. 4 Solar-module parameters during the daytime of September 9, 2020.** The numbers on the right axis are cell values that are calculated from the module and the number of cells, while the actual measurement data of the module belongs to the left axis. While the open-circuit voltage  $V_{oc}$  stays rather constant, the short-circuit current  $j_{sc}$  nearly linearly follows the irradiance curve. The drops in the fill factor FF in the morning and evening can be explained by a low generation current, and the saddle at noontime is due to a high temperature and a huge current density.

three simulation levels. The decreasing behavior of  $V_{oc}$  and FF with rising temperature can be explained by the increasing intrinsic carrier concentration, which is mainly due to the enhanced thermal generation of electron–hole pairs<sup>55</sup>. The short-circuit current is hardly affected by the temperature variation, as can be seen in Supplementary Note 3. These findings agree with previous research and practical experience<sup>56,57</sup>. Since all temperature dependencies are nearly linear, temperature coefficients can be determined. Our simulation reveals values of  $-2.0 \text{ mV K}^{-1}$  and  $-0.06\% \text{ K}^{-1}$ , which are in agreement with measured values of  $-2.1 \text{ mV K}^{-1}$  and  $-0.05\% \text{ K}^{-1}$ <sup>56</sup> and theoretical models ( $-1.6 \text{ mV K}^{-1}$  and  $-0.015\% \text{ K}^{-1}$ )<sup>58</sup>. The detailed calculation of the theoretical values is available in Supplementary Note 3.

The drift-diffusion model is thus calculated with the measured temperature conditions shown in Fig. 2. The corresponding irradiance conditions are fed into the transfer matrix calculation. Finally, Poisson's equation solver is applied to generate the resulting solar-module parameters, which are plotted as orange lines in Fig. 4, together with the experimentally determined data (black dotted). The precise prediction of all three quantities reveals an accurate, holistic model on all three simulation levels.

Several features within the data can be understood and explained by the use of the three-stage simulation model. The open-circuit voltage is mainly constant throughout the entire day. However, for very low irradiance intensities,  $V_{oc}$  does drop due to its logarithmic dependence on the photocurrent. A prominent feature is the increased  $V_{oc}$  in the morning compared to the almost constant value of 95 V for the rest of the day. This can be explained by a low module temperature in the morning. After half past 7, an abrupt increase in irradiance due to sunlight emerging from behind the trees leads to a comparably high current while still maintaining a low module temperature. The result is an increased open-circuit voltage, which relaxes and plateaus while the thermal equilibrium is reached.

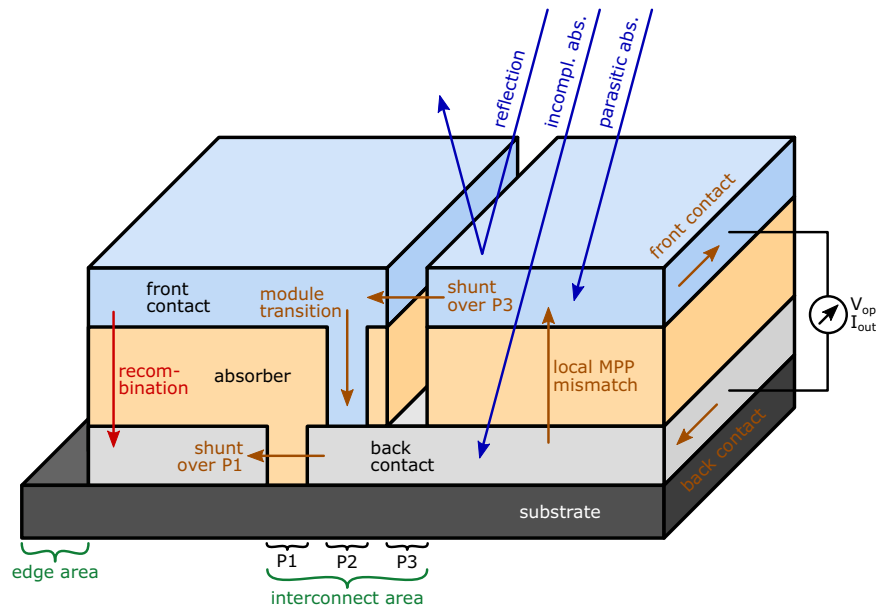


**Fig. 5 Possible losses within a thin-film solar module.** The losses are divided into four categories. Reflection, parasitic absorption, and incomplete absorption form the optical part. Recombination mechanisms are within the electronic portion, while area losses represent the geometrical losses. Electrical losses can be classified into ohmic losses, shunts, and local maximum power point mismatches.

The short-circuit current basically follows the behavior of the irradiance curve in Fig. 2 due to its linear dependence within the transfer-matrix method. This is represented in the simulated data as well as in the experimental data. The dip in the morning due to shadowing by nearby trees is clearly visible within this  $j_{sc}$  graph again.

A notable feature in the plotted fill factor in graph c) is the drop in the early morning and late evening hours. This is due to the low irradiance at this time, which leads to comparably low photocurrents in contrast to the permanently present shunting currents. The dip around noontime is due to two effects. Firstly, according to Fig. 3, the fill factor drops at the higher temperatures present within this time frame. Secondly, the high irradiance at noon implies high current densities. Since the conductivities of the contact layers hardly change with temperature, high currents result in a large potential gradient according to Ohm's law, which is always associated with large electrical losses and hence a lower fill factor.

We studied the same solar-module parameters for a cloudy day (September 6, 2020), which has a much more spiky temperature and illumination behavior throughout the day. Results for this day can be found in Supplementary Note 4. Despite the irregular profile of the operating conditions, we are able to predict  $V_{oc}$ ,  $j_{sc}$ , and FF and, therefore, the generated power with high accuracy.

**Holistic loss analysis from theoretical efficiency limit to actual module yield.** All relevant loss mechanisms that can occur within homogeneous thin-film solar modules are illustrated in Fig. 5. We classified them into four different categories: semiconductor losses, optical losses, geometrical losses, and electrical losses. Each of these classes corresponds to one of the four simulations and calculations described in the section above and illustrated in Fig. 1. While all intrinsic material losses are due to recombination, optical losses can be split into reflection, incomplete absorption (transmission), and parasitic absorption. Their detailed values are determined by the exact number of reflected and absorbed photons within the transfer-matrix approach. Geometrical losses are subdivided into edge area losses, and dead area losses within the monolithic interconnect and can be easily calculated via comparison of areas. Electrical losses have the

largest variety by being split into ohmic losses within all contact layers and module transitions, local MPP mismatches, and shunts across P1 and P3 gaps. All ohmic losses and shunts can be calculated by Ohm's law. The local MPP mismatch is given as the difference of the hypothetically possible produced power without any voltage distribution (each finite element at MPP) and the sum of all actually produced powers of all finite elements<sup>54</sup>.

The upper curve in Fig. 6 is determined from the Shockley-Queisser model<sup>34</sup> via the illumination and the temperature behavior from Fig. 2 and the module area of  $1.2 \times 0.6 \text{ m}^2$  with 144 individual cells. It describes the theoretical maximum power that could be achieved under ideal conditions. For each time step, a coupled simulation of the drift-diffusion model, transfer-matrix method, geometrical calculation, and Poisson's equation solver is performed, and all losses are allocated and quantified. The different colorings in Fig. 6 show the assignment of each loss mechanism. We define the absolute limit of the material as the Shockley-Queisser power minus the recombination losses. This is the maximum power that could be achieved by an optically and electrically ideal module. However, a more realistic limit is an infinitesimally small cell, which contains all optical losses but does not suffer from any electrical transport effects or module area losses. This efficiency limit is at the bottom line of the blue area. Finally, extending a tiny cell towards a real-world module introduces geometrical losses (green) and electrical losses (orange) due to its two-dimensional expansion. Therefore, after subtracting all losses from the Shockley-Queisser limit to the module level, we predict the module to produce the gray colored area as power output. Integrating over the entire day, we calculate that the module will produce 698.9 Wh. Experimental, time-resolved power measurements during the day are plotted as black dots, and the integrated yield is calculated to 698.7 Wh for the entire day, which is in remarkable agreement with the predicted simulated value. This equals a gain of 6.8 kWh per day  $\cdot \text{kW}_p$  for the considered day. Since this was a perfect summer day, this value would be much lower for a simulation over an entire year.

We conclude that with this three-stage simulation model, we are able to accurately simulate real-world thin-film solar modules with all their external influences like temperature and different illumination scenarios and even allocate all losses to their origins.



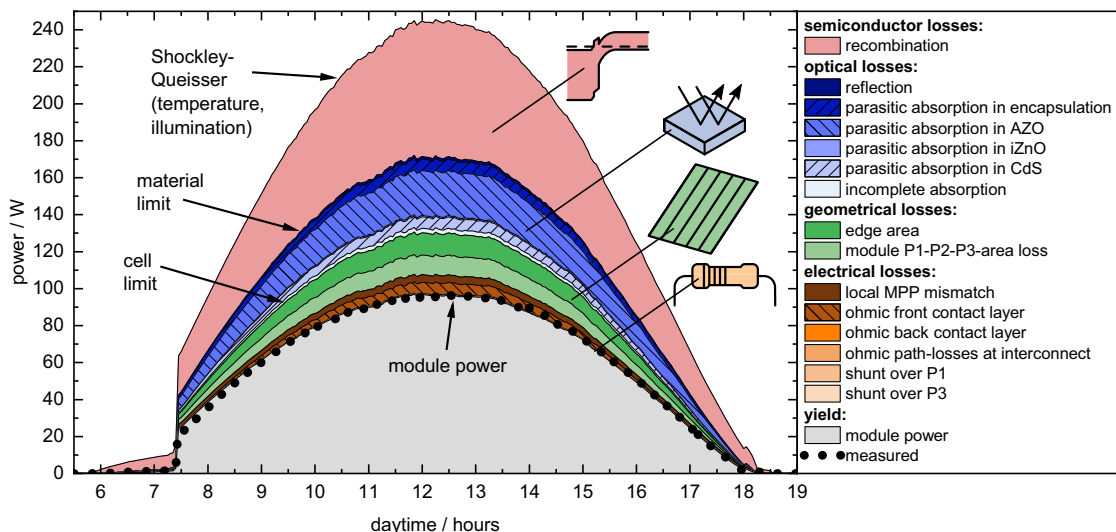


**Fig. 6 Shockley-Queisser model, loss analysis and generated module power during daytime of September 9, 2020.** The material abbreviations CdS, iZnO, and AZO stand for cadmium sulfide, intrinsic zinc oxide, and aluminum-doped zinc oxide, respectively, MPP is the maximum power point, and P1, P2, and P3 are the interconnecting trenches between to serially connected cells. The upper edge of the red area represents the Shockley-Queisser limit for a band gap of 1.13 eV adapted for the module size and the prevailing illumination and temperature. After all losses are identified and quantified, the module is predicted to produce the power indicated within the gray area. Actual measurements in the field are marked as black dots.

To put these results in perspective, we compared the resulting power conversion efficiency (PCE)

$$\text{PCE} = \frac{P_{\text{MPP}}}{P_{\text{in}}} = \frac{V_{\text{MPP}} \cdot I_{\text{MPP}}}{P_{\text{in}}} \quad (1)$$

with the light input power  $P_{\text{in}}$  and the MPP voltage  $V_{\text{MPP}}$ , current  $I_{\text{MPP}}$ , and power  $P_{\text{MPP}}$  of the module with the PCE calculated from the Shockley-Queisser model. Figure 7a shows a colormap of the Shockley-Queisser limit with a band gap of 1.13 eV for a given temperature and irradiance. As can be seen, the Shockley-Queisser model is a variable limit depending on certain input parameters rather than a fixed efficiency limit. As a matter of fact, the PCE limit changes from 29% up to 34%, even within these realistic non-STC conditions. The black line with the blue points represents the trajectory of the operating conditions on the module in the course of the analyzed day September 9, 2020. The projection of the Shockley-Queisser PCE is plotted in Fig. 7b) as a function of time during the day. As in Fig. 6, all losses (colored areas) and the measured module PCE (black dotted) are plotted as well. Since all solar-module parameters in Fig. 4 are simulated accurately, the simulated and measured PCE match quite well.

Low-light conditions in the early morning and late evening hours and heating up around noontime reduce the actual module PCE disproportionately more than the Shockley-Queisser PCE. This can be attributed to the shunt resistances and high temperature coefficients, respectively. Since the PCE is a relative quantity, the simulated values in the early morning and late evening hours don't exactly align with the measured values, but the absolute errors for low intensities are actually extremely small. Moreover, a physical error source might be the absence of a spatially distributed thermal model<sup>59</sup> and assuming a constant equilibrium temperature for the entire module. Since the temperature measurement was performed on the rear side of the module, the actual temperature of the p-n junction might change by up to around 2 K. A loss analysis for laboratory-controlled standard testing conditions can be found in Supplementary Note 5.

**Possible improvements on the module level.** There are many suggestions and realizations of how to improve the light-absorbing material<sup>30,60-66</sup> and, therefore, the entire module performance. Since

the largest single source of loss is recombination, it is reasonable to direct research efforts in this direction. However, this section has its focus on improvements on the module level without touching the absorber material at all. It shall serve as a sensitivity analysis to get a feeling for which parameters have a significant effect on the results and are, therefore, prime targets for future optimization efforts. Many improvements are conceivable, even on complex topological issues like grid pattern optimization<sup>32,67</sup>. However, here we focus on the following points: Reducing sheet resistance in the TCO contact layer, reducing optical absorption in the TCO contact layer, reducing optical absorption in the encapsulant, reducing edge areas, and reducing interconnect areas. As noted in Fig. 1, the actual PCE at STC of the module is 14.27%. In this section, we look for methods to get a PCE gain of 0.65% and hence to 14.92%.

To gain this improvement by reducing electrical losses within the front TCO layer, we can use our simulation to calculate the necessary improvement. We come up with a required TCO sheet resistance of 7.75  $\Omega$  instead of the actual 25  $\Omega$  for the same grid resistivity. Alternatively, the optical losses can be addressed. To achieve the required 0.65%, either the front TCO needs to absorb around 26% less within the relevant wavelength range, or the encapsulant is not allowed to have any parasitic absorption at all. Another way is to reduce the edge area from around 505 cm<sup>2</sup> (7% of the total module) to around 190 cm<sup>2</sup> (2.6% of the total module). The same effect can be achieved by reducing the interconnect area by the same factor from 265  $\mu\text{m}$  in width to 100  $\mu\text{m}$ . To do so, we need to adapt the cell width, as can be seen in Table 2. For the 265  $\mu\text{m}$  of total interconnect width used in the design of our reference module, the cell width is optimized to around 4 mm. However, for 100  $\mu\text{m}$ , the cell width needs to be reduced to 3.5 mm to minimize ohmic losses. Implementing all of the five improvement suggestions mentioned above would improve the efficiency even more than five times 0.65%. In fact, the resulting module would have a PCE of 17.9%, without modifying the CIGS deposition process. This overlap is due to the interactions of the positive effects. For example, a more conductive contact layer material allows the cell to be 4.2 mm in width despite the smaller interconnect area.

This work demonstrates that the physical processes within thin-film solar modules in the field under real application

conditions can be simulated in one three-staged simulation, including a correction for the inactive areas. The three levels of drift-diffusion model, modified transfer-matrix method, and quasi-three-dimensional finite-element Poisson’s equation solver have been linked—to the best of our knowledge—for the first time in literature. We used geometrically, electrically, and optically

measured input data at standard testing conditions (STC) as well as drift-diffusion parameters from the literature. Having established the entire physical model of the module, we can predict solar-module parameters, even for conditions that are far beyond STC, with remarkable agreement. Such simulations can be extended to yield predictions for an entire day based on meteorological data. Due to our holistic device physics, a time-resolved top-down loss analysis from the Shockley–Queisser model to the actual module power can be calculated. Moreover, our sensitivity analysis clearly shows the potential and need for materials with improved optical and electrical properties in order to advance toward higher module efficiencies and to close the gap between cell and module levels. Our reverse engineering fitting (REF) procedure allows us to calculate backward from the module level down to the cell level and even further down to the drift-diffusion level. Parameters that may be difficult to measure experimentally can be determined by this approach.

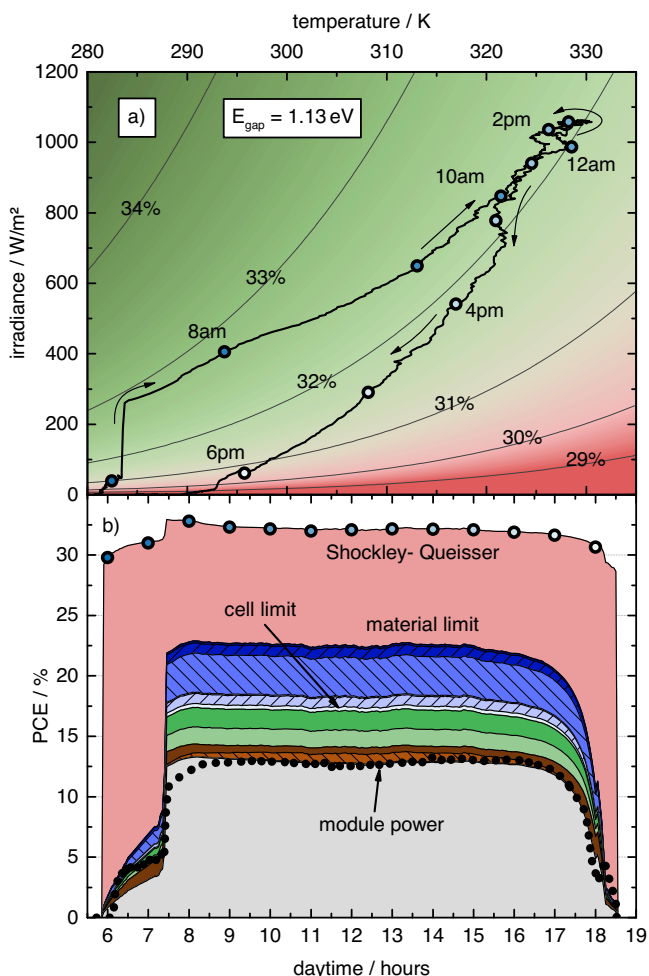


**Fig. 7** Trajectory of the operating conditions of the module within the Shockley-Queisser model during the daytime of September 9, 2020. The Shockley-Queisser limit for a band gap of 1.13 eV is plotted as a colormap in graph a) as a function of temperature and irradiance. The black line represents the course of the conditions during the considered day. The same curve is shown in graph b) in combination with the actual module power conversion efficiency (PCE). All loss mechanisms have the same color coding as in Fig. 6.

**Methods**

**Setting up device simulations.** In this work, we used multiple simulation methods and link them to each other. This is necessary to achieve a holistic physical model starting from the material parameters up to the module level. Using this multi-level simulation procedure, we are able to describe all environmental influences, from temperature effects up to impacts of different illumination conditions.

For the electronic semiconductor simulation, we used a drift-diffusion model within a one-dimensional finite element method<sup>29</sup>. This model solves the van-Roosbroeck system, which is formulated as Poisson’s equation inside the semiconductor and the two continuity equations for electrons and holes. To account for the optics, we used a modified generalized transfer-matrix approach<sup>36</sup> accounting for partially incoherent interference due to rough interfaces<sup>38</sup>. This includes a Lambert–Beer-like absorption for each material within the layer stack as well as internal reflections, back-side reflections, and thin-film interference. Finally, the electrical behavior of the solar modules is considered in Poisson’s equation<sup>39</sup> solver embedded into a quasi-three-dimensional finite element method using a Delaunay-triangulated mesh<sup>40,41</sup>. Finite elements with an active area consist of two electrical potentials on the front and back side and a generating current term which is determined by the drift-diffusion simulation. However, elements within the module interconnection do not have a generating current term but consist of large transport resistances (P1 and P3) or an electrical connection from the front to the back contact (P2). A more detailed description of the simulation techniques can be found in Supplementary Note 2.

**Reverse engineering fitting (REF).** The routine of REF is a special kind of fitting procedure developed for use with simulations instead of an analytical calculation. Since derivatives for any fitting parameter cannot be calculated in this case, the optimization algorithm must be based on a gradient-free procedure. We used our three-stage simulation approach within the loss function of the optimizer, which requires a long runtime for evaluating the function value. Therefore, the efficiency of the optimization algorithm is mainly due to the number of function evaluations, which is why we used a downhill simplex algorithm<sup>68</sup>.

The final goal is to match a simulated I-V curve with experimental I-V data, which is given by  $n$  experimentally measured voltage-current pairs ( $V_i^{exp}, I_i^{exp}$ ). This is achieved by varying the optimization parameters and revealing a simulated I-V curve with also  $n$  voltage-current pairs ( $V_i^{exp}, I_i^{sim}(V_i^{exp})$ ) via the simulation. The final loss

**Table 2** Comparison of ideal cell widths and efficiencies for different improvement implementations described in the main text. In the first row, the standard reference module is used, while in the second row, only the interconnect area was reduced, and in the last row, all improvements are implemented (sheet resistance and transmittance of the transparent conductive oxide (TCO) layer, encapsulant transmittance, interconnect and edge area). All simulated modules have the same area of 1200 × 600 mm<sup>2</sup>. Therefore, the ideal cell width determines the amount of monolithically interconnected cells and hence the absolute module voltage. All optoelectrical parameters are shown, including the open circuit voltage  $V_{oc}$ , short circuit current (density)  $I_{sc}$  and  $j_{sc}$  fill factor FF and power conversion efficiency PCE.

Implemented improvements	interconnect width / $\mu\text{m}$	ideal cell width / mm	# cells	$V_{oc}^{module} / \text{V}$	$V_{oc}^{cell} / \text{V}$	$I_{sc} / \text{A}$	$j_{sc} / \text{mA cm}^{-2}$	FF / %	PCE / %
None	265	4.0	144	103.7	0.720	1.35	27.0	73.4	14.27
Interconnect area	100	3.5	163	117.3	0.719	1.24	28.1	73.8	14.92
All described	100	4.2	136	98.2	0.722	1.34	30.9	80.3	17.90

function for the optimization algorithm is the accumulated mean squared error

$$\chi^2 = \frac{1}{\sum_{i=0}^{n-1} w_i} \cdot \sum_{i=0}^{n-1} w_i \cdot (I_i^{\text{exp}} - I_i^{\text{sim}}(V_i^{\text{exp}}))^2 \quad (2)$$

with the weights  $w_i$  accounting for non-equidistant voltage steps and an exponential current-voltage dependence. As within conventional optimization algorithms, the input parameters are varied as long as a sufficient accuracy within the loss function is reached. In principle, there can be an arbitrary number of fitting parameters. However, in order to converge in a reasonable time scale, only around 4 to 6 free parameters should be used for the downhill simplex algorithm. The reliability of this method is demonstrated in<sup>40</sup>.

**Coefficient of determination.** The coefficient of determination  $R^2$  measures the quality of a fit. To determine this quantity, the ratio of the sum of all residual squares with respect to the sum of all total squares are calculated. The exact calculation is given as

$$R^2 = 1 - \frac{\sum_{i=0}^{N-1} (y_i - p_i)^2}{\sum_{i=0}^{N-1} (y_i - \bar{y})^2} \quad (3)$$

with all  $N$  measured values  $y_i$ , their mean value  $\bar{y} = \frac{1}{N} \sum_{i=0}^{N-1} y_i$ , and the corresponding predicted value  $p_i$ .

**Characterization and measurements.** Experimental data have been collected from an N-G1000E105 CIGS module exposed outdoors at the ZSW test field Widderstall located at 09.713°N, 48.536°E, and 750 m above sea level. It was mounted facing south with a fixed tilt angle of 40° without any tracking. The module was individually characterized in the laboratory by  $I$ - $V$  curve measurement at STC with a class AAA solar flash simulator. During the exposition,  $I$ - $V$  curve scans of the module was conducted and recorded continuously at 1 min intervals by an individual electronic load, which operated the module at MPP between the scans. The plane of array irradiance measurement was performed with a secondary standard pyranometer while the module temperature was measured with a PT1000 resistive sensor at the rear glass surface of the module.

**Module geometry.** The used module has a spatial dimension of 1200 mm × 600 mm. Along the short side, it has an edge area of 19 mm and 9 mm on the top and bottom sides, respectively. The long side is framed by 14.4 mm of edge and contact area on both sides. The active area of 6695 cm<sup>2</sup> is split into 144 monolithically interconnected cells, with 265 μm of interconnect width between the cells. Therefore, all cells are 1172 mm in height and 4 mm in width. The total inactive edge and contact area can be calculated to be 505 cm<sup>2</sup>, which corresponds to around 7% of the total module area.

## Data availability

The data that support the findings of this study are available from the corresponding author upon reasonable request.

## Code availability

The programmed code of this study is available from the corresponding author upon reasonable request.

Received: 29 August 2022; Accepted: 2 March 2023;

Published online: 27 March 2023

## References

- Allouhi, A. et al. Energy consumption and efficiency in buildings: current status and future trends. *J. Clean. Prod.* **109**, 118–130 (2015).
- Cao, X., Dai, X. & Liu, J. Building energy-consumption status worldwide and the state-of-the-art technologies for zero-energy buildings during the past decade. *Energy Build.* **128**, 198–213 (2016).
- Pérez-Lombard, L., Ortiz, J. & Pout, C. A review on buildings energy consumption information. *Energy Build.* **40**, 394–398 (2008).
- Chu, S. & Majumdar, A. Opportunities and challenges for a sustainable energy future. *Nature* **488**, 294–303 (2012).
- Green, M. et al. Solar cell efficiency tables (version 57). *Prog. Photovoltaics* **29**, 3–15 (2020).
- Jackson, P. et al. Properties of Cu(In,Ga)Se<sub>2</sub> solar cells with new record efficiencies up to 21.7%. *Phys. Status Solidi (RRL)* **9**, 28–31 (2015).
- Kayes, B. M. et al. 27.6% Conversion efficiency, a new record for single-junction solar cells under 1 sun illumination. In *37th IEEE Photovoltaic Specialists Conference*, 000004–000008. <https://ieeexplore.ieee.org/document/6185831> (2011).
- Powalla, M. et al. Thin-film solar cells exceeding 22% solar cell efficiency: an overview on CdTe-, Cu(In,Ga)Se<sub>2</sub>-, and perovskite-based materials. *Appl. Phys. Rev.* **5**, 041602 (2018).
- Razykov, T. M. et al. Solar photovoltaic electricity: current status and future prospects. *Sol. Energy* **85**, 1580–1608 (2011).
- Hegedus, S. Thin film solar modules: the low cost, high throughput and versatile alternative to Si wafers. *Prog. Photovolt.* **14**, 393–411 (2006).
- Shah, A. et al. Towards very low-cost mass production of thin-film silicon photovoltaic (PV) solar modules on glass. *Thin Solid Films* **502**, 292–299 (2006).
- Peng, J. et al. Centimetre-scale perovskite solar cells with fill factors of more than 86 per cent. *Nature* **601**, 573–578 (2022).
- Kayes, B. M., Zhang, L., Twist, R., Ding, I.-K. & Higashi, G. S. Flexible thin-film tandem solar cells with >30% efficiency. *IEEE J. Photovolt.* **4**, 729–733 (2014).
- Gaillard, N. et al. Wide-bandgap Cu (In, Ga) S<sub>2</sub> photocathodes integrated on transparent conductive F: SnO<sub>2</sub> substrates for photocopyrite-based water splitting tandem devices. *ACS Appl. Energy Mater.* **2**, 5515–5524 (2019).
- Schultes, M. et al. Sputtered transparent electrodes (IO:H and IZO) with low parasitic near-infrared absorption for perovskite–Cu(In,Ga)Se<sub>2</sub> tandem solar cells. *ACS Appl. Energy Mater.* **2**, 7823–7831 (2019).
- Al-Ashouri, A. et al. Monolithic perovskite/silicon tandem solar cell with >29% efficiency by enhanced hole extraction. *Science* **370**, 1300–1309 (2020).
- Septina, W. et al. In situ Al<sub>2</sub>O<sub>3</sub> incorporation enhances the efficiency of CuIn (S, Se) 2 solar cells prepared from molecular-ink solutions. *J. Mater. Chem. A* **9**, 10419–10426 (2021).
- Jacobsson, T. J., Fjällström, V., Sahlberg, M., Edoff, M. & Edvinsson, T. A monolithic device for solar water splitting based on series interconnected thin film absorbers reaching over 10% solar-to-hydrogen efficiency. *Energy Environ. Sci.* **6**, 3676–3683 (2013).
- Gaillard, N., Prasher, D., Kaneshiro, J., Mallory, S. & Chong, M. Development of chalco-genide thin film materials for photoelectrochemical hydrogen production. *MRS Online Proceedings Library (OPL)* 1558. <https://link.springer.com/article/10.1557/opl.2013.1084> (2013).
- Lee, C. H., Kim, D. R. & Zheng, X. Transfer printing methods for flexible thin film solar cells: Basic concepts and working principles. *ACS Nano* **8**, 8746–8756 (2014).
- Powalla, M. et al. CIGS cells and modules with high efficiency on glass and flexible substrates. *IEEE J. Photovolt.* **4**, 440–446 (2013).
- Moon, S., Kim, K., Kim, Y., Heo, J. & Lee, J. Highly efficient single-junction GaAs thin-film solar cell on flexible substrate. *Sci. Rep.* **6**, 1–6 (2016).
- Grübel, B. et al. Progress of plated metallization for industrial bifacial TOPCon silicon solar cells. *Prog. Photovolt.* **30**, 615–621 (2022).
- Yoshikawa, K. et al. Silicon heterojunction solar cell with interdigitated back contacts for a photoconversion efficiency over 26%. *Nat. Energy* **2**, 17032 (2017).
- Richter, A. et al. Design rules for high-efficiency both-sides-contacted silicon solar cells with balanced charge carrier transport and recombination losses. *Nat. Energy* **6**, 429–438 (2021).
- Pieters, B. E. & Rau, U. A new 2D model for the electrical potential in a cell stripe in thin-film solar modules including local defects. *Prog. Photovolt.* **23**, 331–339 (2015).
- Fecher, F. W., Romero, A. P., Brabec, C. J. & Buerhop-Lutz, C. Influence of a shunt on the electrical behavior in thin film photovoltaic modules—a 2D finite element simulation study. *Sol. Energy* **105**, 494–504 (2014).
- Kikelj, M., Lipovšek, B., Bokalič, M. & Topič, M. Spatially resolved electrical modelling of cracks and other inhomogeneities in crystalline silicon solar cells. *Prog. Photovolt.* **29**, 124–133 (2021).
- Burgelman, M., Nolle, P. & Degraeve, S. Modelling polycrystalline semiconductor solar cells. *Thin Solid Films* **361–362**, 527–532 (2000).
- Topič, M., Smole, F. & Furlan, J. Band-gap engineering in Cds/Cu (In, Ga) Se<sub>2</sub> solar cells. *J. Appl. Phys.* **79**, 8537–8540 (1996).
- Bermudez, V. & Perez-Rodriguez, A. Understanding the cell-to-module efficiency gap in Cu(In,Ga)(S,Se)<sub>2</sub> photovoltaics scale-up. *Nat. Energy* **3**, 466–475 (2018).
- Zinßer, M. et al. Irradiation-dependent topology optimization of metallization grid patterns used for latitude-based yield gain of thin-film solar modules. *MRS Adv.* **7**, 706–712 (2022).
- Pfreundt, A., Shahid, J. & Mittag, M. Cell-to-module Analysis beyond Standard Test Conditions. In *47th IEEE Photovoltaic Specialists Conference (PVSC)*, 0921–0926 (IEEE, 2020). <https://ieeexplore.ieee.org/abstract/document/9300684>.
- Shockley, W. & Queisser, H. J. Detailed balance limit of efficiency of p-n junction solar cells. *J. Appl. Phys.* **32**, 510–519 (1961).
- Guillemoles, J.-F., Kirchartz, T., Cahen, D. & Rau, U. Guide for the perplexed to the Shockley–Queisser model for solar cells. *Nat. Photonics* **13**, 501–505 (2019).



36. Byrnes, S. J. *Multilayer Optical Calculations*. Preprint at *arXiv* <https://arxiv.org/abs/1603.02720> (2020).
37. Carron, R. et al. Refractive indices of layers and optical simulations of Cu(In,Ga)Se<sub>2</sub> solar cells. *Sci. Technol. Adv. Mater.* **19**, 396–410 (2018).
38. Katsidis, C. C. & Siapakas, D. I. General transfer-matrix method for optical multilayer systems with coherent, partially coherent, and incoherent interference. *Appl. Opt.* **41**, 3978–3987 (2002).
39. Poisson, S. D. Mémoire sur la théorie du magnétisme en mouvement. *Mém. Acad. R. Sci.* **6**, 441–570 (1823).
40. Zinßer, M. et al. Finite element simulation of electrical intradevice physics of thin-film solar cells and its implications on the efficiency. *IEEE J. Photovolt.* **12**, 483–492 (2022).
41. Zinßer, M. et al. Optical and electrical loss analysis of thin-film solar cells combining the methods of transfer-matrix and finite elements. *IEEE J. Photovolt.* **12**, 1154–1161 (2022).
42. Paulson, P. D., Stephens, S. H. & Shafarman, W. N. Analysis of Cu (In,Ga) Se<sub>2</sub> alloy film optical properties and the effect of Cu off-Stoichiometry. *MRS Online Proc. Libr.* **865**, 141–146 (2004).
43. Minoura, S. et al. Optical constants of Cu(In,Ga)Se<sub>2</sub> for arbitrary Cu and Ga compositions. *J. Appl. Phys.* **117**, 195703 (2015).
44. Zinßer, M. *Numerically Robust Methodology for Fitting Current-Voltage Characteristics of Solar Devices with the Single-Diode Equivalent-Circuit Model*. Preprint at *arXiv* <https://arxiv.org/abs/2206.13087> (2022).
45. Meyer, E. L. & Van Dyk, E. E. The effect of reduced shunt resistance and shading on photovoltaic module performance. In *Conference Record of the Thirty-first IEEE Photovoltaic Specialists Conference, 2005*. 1331–1334 (IEEE, 2005). <https://ieeexplore.ieee.org/document/1488387>.
46. Boukourt, N. E. I., Patané, S., Adouane, M. & AlHammadi, R. Numerical optimization of ultrathin CIGS solar cells with rear surface passivation. *Sol. Energy* **220**, 590–597 (2021).
47. Diaz-Loera, A., Ramos-Serrano, J. R. & Calixto, M. E. Semiconducting CuIn(S<sub>x</sub>Se<sub>1-x</sub>)<sub>2</sub> thin-film solar cells modeling using SCAPS-1D. *MRS Adv.* **7**, 28–32 (2022).
48. Malm, U. & Edoff, M. 2D device modelling and finite element simulations for thin-film solar cells. *Sol. Energy Mater. Sol. Cells* **93**, 1066–1069 (2009).
49. Sun, X., Silverman, T., Garris, R., Deline, C. & Alam, M. A. An illumination- and temperature-dependent analytical model for copper indium gallium diselenide (CIGS) solar cells. *IEEE J. Photovolt.* **6**, 1298–1307 (2016).
50. Sozzi, G. et al. Influence of conduction band offsets at window/buffer and buffer/absorber interfaces on the roll-over of JV curves of CIGS solar cells. In *IEEE 44th Photovoltaic Specialist Conference (PVSC), 2205–2208* (IEEE, 2017). <https://ieeexplore.ieee.org/abstract/document/8366649>.
51. Mostefaoui, M., Mazari, H., Khelifi, S., Bouraoui, A. & Dabou, R. Simulation of high efficiency CIGS solar cells with SCAPS-1D software. *Energy Proc.* **74**, 736–744 (2015).
52. Yamaguchi, M. et al. Analysis for non-radiative recombination and resistance loss in chalcopyrite and kesterite solar cells. *Jpn. J. Appl. Phys.* **60**, SBBF05 (2021).
53. Kato, T., Wu, J.-L., Hirai, Y., Sugimoto, H. & Bermudez, V. Record efficiency for thin-film polycrystalline solar cells up to 22.9% achieved by Cs-treated Cu(In,Ga)(Se,S)<sub>2</sub>. *IEEE J. Photovolt.* **9**, 325–330 (2018).
54. Wächter, R., Kaune, G., Repmann, T. & Orgassa, K. Loss analysis and efficiency potentials for CIGS thin-film PV modules without and with metal grid: Experimental results analyzed by simulation. In *37th European Photovoltaic Solar Energy Conference and Exhibition*, 3–936338–73–6. <https://www.eupvsec-proceedings.com/proceedings?paper=49221> (2020).
55. Wenham, S. R., Green, M. A., Watt, M. E., Corkish, R. & Sproul, A. *Applied Photovoltaics* (Routledge, 2013). <https://www.taylorfrancis.com/books/mono/10.4324/9781849776981/applied-photovoltaics-stuart-wenham-martin-green-muriel-watt-richard-corkish-alistair-sproul>.
56. Theelen, M. et al. Determination of the temperature dependency of the electrical parameters of CIGS solar cells. *J. Renew. Sustain. Energy* **9**, 021205 (2017).
57. Meneses-Rodriguez, D., Horley, P. P., Gonzalez-Hernandez, J., Vorobiev, Y. V. & Gorley, P. N. Photovoltaic solar cells performance at elevated temperatures. *Sol. Energy* **78**, 243–250 (2005).
58. Singh, P. & Ravindra, N. M. Temperature dependence of solar cell performance - an analysis. *Sol. Energy Mater. Sol. Cells* **101**, 36–45 (2012).
59. Mittag, M., Vogt, L., Herzog, C. & Neuhaus, H. Thermal modelling of photovoltaic modules in operation and production. In *36th European Photovoltaic Solar Energy Conference and Exhibition (EUPVSEC)*. [https://www.ise.fraunhofer.de/content/dam/ise/de/documents/publications/conference-paper/36-eupvsec-2019/Mittag\\_4CO24.pdf](https://www.ise.fraunhofer.de/content/dam/ise/de/documents/publications/conference-paper/36-eupvsec-2019/Mittag_4CO24.pdf) (2019).
60. Siebentritt, S. What limits the efficiency of chalcopyrite solar cells? *Sol. Energy Mater. Sol. Cells* **95**, 1471–1476 (2011).
61. Lundberg, O., Edoff, M. & Stolt, L. The effect of Ga-grading in CIGS thin film solar cells. *Thin Solid Films* **480**, 520–525 (2005).
62. Jackson, P. et al. Effects of heavy alkali elements in Cu (In, Ga) Se<sub>2</sub> solar cells with efficiencies up to 22.6%. *Phys. Status Solidi* **10**, 583–586 (2016).
63. Carron, R. et al. Advanced alkali treatments for high-efficiency Cu(In,Ga)Se<sub>2</sub> solar cells on flexible substrates. *Adv. Energy Mater.* **9**, 1900408 (2019).
64. Helder, T. et al. DLTS investigations on CIGS solar cells from an inline co-evaporation system with RbF post-deposition treatment. *EPJ Photovolt.* **13**, 7 (2022).
65. Lindahl, J. et al. Inline Cu(In,Ga)Se<sub>2</sub> Co-evaporation for high-efficiency solar cells and modules. *IEEE J. Photovolt.* **3**, 1100–1105 (2013).
66. Kanevce, A., Paetel, S., Hariskos, D. & Magorian Friedlmeier, T. Impact of RbF-PDT on Cu(In,Ga)Se<sub>2</sub> solar cells with CdS and Zn(O,S) buffer layers. *EPJ Photovolt.* **11**, 8 (2020).
67. Gupta, D. K., Langelaar, M., Barink, M. & van Keulen, F. Topology optimization of front metallization patterns for solar cells. *Struct. Multidiscip. Optim.* **51**, 941–955 (2015).
68. Nelder, J. A. & Mead, R. A simplex method for function minimization. *Comput. J.* **7**, 308–313 (1965).
69. Witte, W. et al. Gallium gradients in Cu(In,Ga)Se<sub>2</sub> thin-film solar cells. *Prog. Photovolt.* **23**, 717–733 (2015).
70. Richter, M., Hammer, M., Sonnet, T. & Parisi, J. Bandgap extraction from quantum efficiency spectra of Cu(In,Ga)Se<sub>2</sub> solar cells with varied grading profile and diffusion length. *Thin Solid Films* **633**, 213–217 (2017).

## Acknowledgements

This work was supported by the German Federal Ministry for Economic Affairs and Climate Action (BMWK) under the contract number 0324353A (CIGSTheoMax), the German Academic Scholarship Foundation, and the Ministry of Science, Research and the Arts of Baden-Württemberg as part of the sustainability financing of the projects of the Excellence Initiative II. The authors acknowledge fruitful and productive discussions with Ana Kanevce, Stefan Paetel, Jan-Philipp Becker, and Erwin Lotter as well as the provision of the experimental data by Dirk Stellbogen.

## Author contributions

M.Z. developed the REF procedure, did all the analysis, and wrote the paper, with all authors contributing feedback and comments. M.Z. and T.H. programmed the tools and conducted all the simulations, with supervision from A.B. T.M.F. contributed crucial ideas in merging simulations with experimental data and internally reviewed the manuscript. T.K. and U.R. provided the expertise in the theoretical calculations of this work. R.W. provided expertise in the designing and measuring of the solar module. M.P. directed and supervised the study.

## Funding

Open Access funding enabled and organized by Projekt DEAL.

## Competing interests

The authors declare no competing interests.

## Additional information

**Supplementary information** The online version contains supplementary material available at <https://doi.org/10.1038/s42005-023-01164-6>.

**Correspondence** and requests for materials should be addressed to Mario Zinßer.

**Peer review information** *Communications Physics* thanks Susanne Siebentritt and the other, anonymous, reviewer(s) for their contribution to the peer review of this work. Peer reviewer reports are available.

**Reprints and permission information** is available at <http://www.nature.com/reprints>

**Publisher's note** Springer Nature remains neutral with regard to jurisdictional claims in published maps and institutional affiliations.



**Open Access** This article is licensed under a Creative Commons Attribution 4.0 International License, which permits use, sharing, adaptation, distribution and reproduction in any medium or format, as long as you give appropriate credit to the original author(s) and the source, provide a link to the Creative Commons license, and indicate if changes were made. The images or other third party material in this article are included in the article's Creative Commons license, unless indicated otherwise in a credit line to the material. If material is not included in the article's Creative Commons license and your intended use is not permitted by statutory regulation or exceeds the permitted use, you will need to obtain permission directly from the copyright holder. To view a copy of this license, visit <http://creativecommons.org/licenses/by/4.0/>.

© The Author(s) 2023